



ELSEVIER

Contents lists available at ScienceDirect

Journal of Computational Physics

www.elsevier.com/locate/jcp



Exponential versus IMEX high-order time integrators for thermal convection in rotating spherical shells



Ferran Garcia^{a,*}, Luca Bonaventura^b, Marta Net^a, Juan Sánchez^a

^a Departament de Física Aplicada, Universitat Politècnica de Catalunya, Jordi Girona 1-3, 08034 Barcelona, Spain

^b MOX – Modelling and Scientific Computing, Dipartimento di Matematica “F. Brioschi”, Politecnico di Milano, Via Bonardi 9, 20133 Milano, Italy

ARTICLE INFO

Article history:

Received 28 July 2013

Received in revised form 20 December 2013

Accepted 22 January 2014

Available online 24 January 2014

Keywords:

Exponential integrators

Semi-implicit schemes

Geophysical modeling

Thermal convection

Low Ekman number flows

ABSTRACT

We assess the accuracy and efficiency of several exponential time integration methods coupled to a spectral discretization of the three-dimensional Boussinesq thermal convection equations in rotating spherical shells. Exponential methods are compared to implicit–explicit (IMEX) multi-step methods already studied previously in [1]. The results of a wide range of numerical simulations highlight the superior accuracy of exponential methods for a given time step, especially when employed with large time steps and at low Ekman number. However, presently available implementations of exponential methods appear to be in general computationally more expensive than those of IMEX methods and further research is needed to reduce their computational cost per time step. A physically justified extrapolation argument suggests that some exponential methods could be the most efficient option for integrating flows near Earth’s outer core conditions.

© 2014 Elsevier Inc. All rights reserved.

1. Introduction

Spectral (or, more accurately, pseudospectral) spatial discretizations are an established tool for problems in spherical geometry, see e.g. [2–5]. Due to the very high accuracy of such a space discretization method, the application of high order methods in time is meaningful and appropriate, in order to achieve the goal of minimizing both space and time truncation errors. On the other hand, for typical problems in spherical geometry in which spectral discretizations are employed, such as atmospheric modeling and mantle convection, extreme efficiency is mandatory, due to the need to carry out simulations on very long time scales. For these reasons, the numerical methods to be preferred should allow the use of relatively large time steps, while maintaining a high level of accuracy. In this work we assess the accuracy and efficiency of some high order exponential time integrators for spectral discretizations of thermal convection equations in spherical geometry. We extend previous works [1,6], where high order IMEX methods [7,8] were considered and their accuracy and efficiency evaluated.

Exponential integrators are an attractive technique for time discretization of systems of ordinary differential equations (ODEs). In the case of a linear, homogeneous Cauchy problem $\dot{\mathbf{x}} = \mathbf{A}\mathbf{x}$, $\mathbf{x}(0) = \mathbf{x}_0$, they consist in the numerical approximation of the solution representation formula $\mathbf{x}(t) = \exp(\mathbf{A}t)\mathbf{x}_0$. As long as the exponential matrix can be computed accurately, this approach can be extended to obtain methods for nonlinear equations that are linearly unconditionally stable and provide the exact solution for linear ODE systems. Early methods of this type were proposed already in the late 1960s, see e.g. [9]. Accurate and reliable computation of the exponential matrix, however, is not an easy task, as discussed in the well known review [10]. In particular, for a long time these methods have been inapplicable to large ODE systems deriving from the spatial discretizations of partial differential equations. On the other hand, starting with the seminal paper by Y. Saad [11], Krylov space methods have established themselves as an advantageous option for this type of applications. Since then, an

* Corresponding author.

increasing attention has been devoted to the use of this technique for stiff problems and large scale computational problems have been successfully solved by these methods, see e.g. the results in [12,13]. Recent reviews and assessment of exponential methods can be found, among others, in [14–16], while other applications of exponential methods to thermal convection problems can be found in [17].

In this paper, we will focus especially on the application of the so called exponential Rosenbrock methods proposed in [18], which have already been applied to large scale fluid dynamics simulations in [13]. A wide range of numerical simulations clearly show that such exponential methods are more accurate by at least one order of magnitude than the equivalent order IMEX scheme. This is especially true when they are employed with large time steps and at small Ekman number. On the other hand, presently available implementations of exponential methods appear to be in general computationally more expensive than those of IMEX methods, although in the small Ekman number limit they tend to be competitive also in terms of computational cost. Therefore, since the small Ekman number regime is among the most physically relevant for mantle convection problems, application of exponential methods appears to be very promising for this kind of applications. Indeed, a physically justified extrapolation argument seems to hint that the exponential time differencing Rosenbrock methods (ETDR) could be the most efficient option for integrating flows near Earth outer core conditions.

The paper is organized as follows. In Section 2, the model equations and the spectral space discretization are introduced. In Section 3 the time integration methods are presented in detail, while in Section 4 the numerical simulations performed are shown and discussed. Some conclusions and perspectives for future work are summarized in Section 6.

2. The model equations and the spectral space discretization

We consider the thermal convection of a differentially heated spherical fluid shell, rotating about an axis of symmetry with constant angular velocity $\boldsymbol{\Omega} = \Omega \mathbf{k}$ and subject to radial gravity $\mathbf{g} = -\gamma \mathbf{r}$, where γ is a constant and \mathbf{r} the position vector. We write below the mass, momentum and energy equations in a rotating frame of reference with angular velocity $\boldsymbol{\Omega}$, using the same formulation and non-dimensional units as in [1]. The units employed are the gap width, $d = r_o - r_i$, for the distance, $v^2/\gamma\alpha d^4$ for the temperature, and d^2/ν for time, r_i and r_o being the inner and outer radii, respectively, ν the kinematic viscosity, and α the thermal expansion coefficient. The velocity field is expressed in terms of toroidal, Ψ , and poloidal, Φ , potentials as

$$\mathbf{v} = \nabla \times (\Psi \mathbf{r}) + \nabla \times \nabla \times (\Phi \mathbf{r}). \quad (1)$$

Consequently, the equations for both potentials, and the temperature perturbation, $\Theta = T - T_c$, from the conduction state $\mathbf{v} = \mathbf{0}$, $T = T_c(r)$, with $r = \|\mathbf{r}\|_2$, are

$$\left[(\partial_t - \nabla^2) L_2 - \frac{2}{E} \partial_\varphi \right] \Psi = -\frac{2}{E} \mathcal{Q} \Phi - \mathbf{r} \cdot \nabla \times (\boldsymbol{\omega} \times \mathbf{v}), \quad (2)$$

$$\left[(\partial_t - \nabla^2) L_2 - \frac{2}{E} \partial_\varphi \right] \nabla^2 \Phi + L_2 \Theta = \frac{2}{E} \mathcal{Q} \Psi + \mathbf{r} \cdot \nabla \times \nabla \times (\boldsymbol{\omega} \times \mathbf{v}), \quad (3)$$

$$(\sigma \partial_t - \nabla^2) \Theta - R \eta (1 - \eta)^{-2} r^{-3} L_2 \Phi = -\sigma (\mathbf{v} \cdot \nabla) \Theta. \quad (4)$$

Here $\boldsymbol{\omega} = \nabla \times \mathbf{v}$ is the vorticity, R is the Rayleigh number, σ the Prandtl number, E the Ekman number and η is the radius ratio. These non-dimensional parameters are defined in this context as

$$R = \frac{\gamma \alpha \Delta T d^4}{\kappa \nu}, \quad E = \frac{\nu}{\Omega d^2}, \quad \sigma = \frac{\nu}{\kappa}, \quad \eta = \frac{r_i}{r_o}, \quad (5)$$

where κ is the thermal diffusivity, and ΔT the temperature difference between the inner and outer boundaries. The operators L_2 and \mathcal{Q} are defined by $L_2 \equiv -r^2 \nabla^2 + \partial_r (r^2 \partial_r)$, $\mathcal{Q} \equiv r \cos \theta \nabla^2 - (L_2 + r \partial_r) (\cos \theta \partial_r - r^{-1} \sin \theta \partial_\theta)$, (r, θ, φ) being the spherical coordinates, with θ measuring the colatitude, and φ the longitude. In non-dimensional units the conduction state reads $T_c(r) = T_0 + R \eta / \sigma (1 - \eta)^2 r$. Non-slip, perfect thermally conducting conditions $\Phi = \partial_r \Phi = \Psi = \Theta = 0$ are assigned at the internal and external boundaries.

A standard treatment of the spatial dependence of the equations is used, so that we will only discuss the basic points (see, e.g., [19,20] for more details). The functions $X = (\Psi, \Phi, \Theta)$ are expanded in spherical harmonic series up to degree L , namely

$$X(t, r, \theta, \varphi) = \sum_{l=0}^L \sum_{m=-l}^l X_l^m(r, t) Y_l^m(\theta, \varphi), \quad (6)$$

with $\Psi_l^{-m} = \overline{\Psi_l^m}$, $\Phi_l^{-m} = \overline{\Phi_l^m}$, $\Theta_l^{-m} = \overline{\Theta_l^m}$, $\Psi_0^0 = \Phi_0^0 = \Theta_0^0 = 0$ to uniquely determine the two scalar potentials, and $Y_l^m(\theta, \varphi) = P_l^m(\cos \theta) e^{im\varphi}$, P_l^m being the normalized associated Legendre functions of degree l and order m . Eqs. (2)–(4) written for the complex coefficients become

$$\partial_t \Psi_l^m = \mathcal{D}_l \Psi_l^m + \frac{1}{l(l+1)} [2E^{-1}(im\Psi_l^m - [\mathcal{Q}\Phi]_l^m) - [\mathbf{r} \cdot \nabla \times (\boldsymbol{\omega} \times \mathbf{v})]_l^m], \tag{7}$$

$$\partial_t \mathcal{D}_l \Phi_l^m = \mathcal{D}_l^2 \Phi_l^m - \Theta_l^m + \frac{1}{l(l+1)} [2E^{-1}(im\mathcal{D}_l \Phi_l^m + [\mathcal{Q}\Psi]_l^m) + [\mathbf{r} \cdot \nabla \times \nabla \times (\boldsymbol{\omega} \times \mathbf{v})]_l^m], \tag{8}$$

$$\partial_t \Theta_l^m = \sigma^{-1} \mathcal{D}_l \Theta_l^m + \sigma^{-1} l(l+1) R \eta (1-\eta)^{-2} r^{-3} \Phi_l^m - [(\mathbf{v} \cdot \nabla) \Theta]_l^m, \tag{9}$$

with boundary conditions

$$\Psi_l^m = \Phi_l^m = \partial_r \Phi_l^m = \Theta_l^m = 0. \tag{10}$$

The spherical harmonic coefficients of the operator $\mathcal{Q} = \mathcal{Q}^u + \mathcal{Q}^l$ are

$$\begin{aligned} [\mathcal{Q}^u f]_l^m &= -l(l+2)c_{l+1}^m D_{l+2}^+ f_{l+1}^m, \\ [\mathcal{Q}^l f]_l^m &= -(l-1)(l+1)c_l^m D_{1-l}^+ f_{l-1}^m, \end{aligned} \tag{11}$$

where we have set

$$D_l^+ = \partial_r + \frac{l}{r}, \quad c_l^m = \left(\frac{l^2 - m^2}{4l^2 - 1} \right)^{1/2}, \quad \mathcal{D}_l = \partial_{rr}^2 + \frac{2}{r} \partial_r - \frac{l(l+1)}{r^2}. \tag{12}$$

In the radial direction, a collocation method is employed, using a Gauss–Lobatto mesh of $N_r + 1$ points ($N_r - 1$ being the number of inner points).

The spherical harmonic coefficients of the nonlinear terms in Eqs. (7)–(9) are obtained following [19]. The velocity and vorticity fields are computed first on a collocation mesh in the three coordinates (r, θ, φ) with the help of dealiased Legendre and fast Fourier transforms [3]. The cross product is computed on the mesh, and, finally, transformed back to the spectral space in the angular variables. The computation of the coefficients of the nonlinear terms of Eq. (9) requires the evaluation of the inner product $(\mathbf{v} \cdot \nabla)\Theta$ on the collocation mesh, and then to transform back to the spectral space.

The mode $m = l = 0$ is nonzero only for Θ to uniquely determine Ψ and Φ , while the amplitudes for $m = 0$ are real. With these considerations, a large system of ordinary differential equations of dimension $N = (3L^2 + 6L + 1)(N_r - 1)$ must be integrated in time.

3. Time integration methods

In this section, we introduce the two different classes of methods for integrating stiff ordinary differential equations that have been considered in this paper, namely the IMEX backward differentiation formulae (IMEX-BDF) [7,8,21] and the exponential time differencing schemes (ETD) [15,18,22,23]. To describe these time integration methods, Eqs. (7)–(9) are written in the form

$$\mathcal{L}_0 \dot{u} = \mathcal{L}u + \mathcal{N}(u), \tag{13}$$

where $u = (\Psi_l^m(r_i), \Phi_l^m(r_i), \Theta_l^m(r_i))$ is the vector containing the values of the spherical harmonic coefficients at the inner radial collocation points, and \mathcal{L}_0 and \mathcal{L} are linear operators including the boundary conditions. The former is invertible. Its action is that of the identity for the Ψ_l^m and Θ_l^m components, while it is defined by the operator \mathcal{D}_l for the component Φ_l^m (see the time derivatives in Eqs. (7)–(9)). In the ETD schemes, the operator \mathcal{L} includes all the linear terms, while in the IMEX-BDF scheme it only includes the terms $\mathcal{D}_l \Psi_l^m$, $\mathcal{D}_l^2 \Phi_l^m - \Theta_l^m$, and $\sigma^{-1} \mathcal{D}_l \Theta_l^m + \sigma^{-1} l(l+1) R \eta (1-\eta)^{-2} r^{-3} \Phi_l^m$ of Eqs. (7), (8) and (9), respectively, and part of the Coriolis terms (see below). In the IMEX-BDF scheme the operator \mathcal{N} , which is treated explicitly, always contains the nonlinear terms and the part of the Coriolis terms not included in \mathcal{L} . In the ETD scheme, the operator \mathcal{N} only contains the nonlinear terms. All the time integration methods defined in the following will be assumed to provide approximations $u^n \approx u(t_n)$ to solutions of Eq. (13) at time levels $t_n = t_{n-1} + \Delta t_{n-1}$, $n = 1, 2, \dots, M$.

3.1. Implicit–explicit schemes

The IMEX-BDF schemes employed here were described in detail in [1,6] so only a very short description will be included here. IMEX-BDF schemes are collocation multistep methods, which obtain u^{n+1} from the previous approximations u^{n-j} , $j = 0, 1, \dots, k-1$, k being the number of steps in the formula. When constant time steps $\Delta t_n = h$ are considered, the linear system to be solved in order to find u^{n+1} can be expressed as

$$\left(\mathcal{I} - \frac{h}{\gamma_0} \mathcal{L}_0^{-1} \mathcal{L} \right) u^{n+1} = \sum_{i=0}^{k-1} \frac{\alpha_i}{\gamma_0} u^{n-i} + \sum_{i=0}^{k-1} \frac{\beta_i h}{\gamma_0} \mathcal{L}_0^{-1} \mathcal{N}(u^{n-i}), \tag{14}$$

where the coefficients α_i , β_j and γ_0 do not depend on n , and are listed, for instance, in [24]. It is well known that, if $k \leq 6$ and the time steps are constant (see e.g. [25, §III.3]), the BDF formulae are zero-stable, while they are unstable for $k \geq 7$. It

is also known that for $k \leq 6$ the k -step formula is convergent of order k , that is, the errors $u(t_n) - u^n$ are $O(h^k)$. Therefore the k -step formula is also termed the k -th order formula.

We have chosen the Q -splitting IMEX-BDF method of [1,6] because it had the best performance among the methods analyzed in fixed time step numerical tests. In this scheme, one step is performed by taking \mathcal{Q}^u of Eq. (11) implicitly (including it in the operator \mathcal{L} of Eq. (13)), and \mathcal{Q}^l of Eq. (11) explicitly (including it in the operator \mathcal{N} of Eq. (13)), while the opposite is done the next step. The rest of the linear operators are always treated implicitly and the nonlinear operator explicitly.

This study is restricted to fixed time step methods, although for comparison purposes results using variable step-size and variable order (VSVO) IMEX-BDF implementation are included in the efficiency plots of Sections 4.1 and 4.2. See [1] for details on this algorithm.

3.2. Exponential time differencing schemes

To describe the ETD schemes, Eq. (13) is written in the form

$$\dot{u} = \mathcal{L}_0^{-1} \mathcal{L}u + \mathcal{L}_0^{-1} \mathcal{N}(u) = \mathcal{F}(u), \quad (15)$$

where \mathcal{L} contains the linear terms (including the Coriolis term) and \mathcal{N} the nonlinear terms of Eqs. (7)–(9).

We have considered first the ETD schemes of orders 2 to 4 as described in [18]. The ETD scheme of second order (ETDR2) is defined by the formula

$$u^{n+1} = u^n + h\varphi(hA)\mathcal{F}(u^n), \quad (16)$$

where $h = t_{n+1} - t_n$, \mathcal{F} is the right-hand side of Eq. (13), $\varphi(z) = (e^z - 1)/z$ and $A = \mathcal{J}(u^n)$, where \mathcal{J} denotes the Jacobian of the right hand side of Eq. (15)

$$\mathcal{J}(u) = \mathcal{L}_0^{-1} \mathcal{L} + \mathcal{L}_0^{-1} \frac{\partial \mathcal{N}}{\partial u}(u) = \frac{\partial \mathcal{F}}{\partial u}(u).$$

In our implementation, we either compute the action of the Jacobian of the nonlinear operator on a vector v by the one-sided approximation

$$\left(\frac{\partial \mathcal{N}}{\partial u}(u) \right)(v) \approx \frac{\mathcal{N}(u + \epsilon v) - \mathcal{N}(u)}{\epsilon} \quad (17)$$

with, as usual, $\epsilon = \|u\|_2 \sqrt{\epsilon_{mach}}$, ϵ_{mach} being an estimate of the round-off error, or by the centered formula

$$\left(\frac{\partial \mathcal{N}}{\partial v}(u) \right)(v) = \frac{1}{2\epsilon} [\mathcal{N}(u + \epsilon v) - \mathcal{N}(u - \epsilon v)], \quad (18)$$

which is exact for a quadratic \mathcal{N} , except for rounding errors. In this case we have always taken $\epsilon = 1$ to reduce them. More information on when they have been used is given below in this section, and at the end of Section 5.

Among the family of ETD schemes of third order (ETDR3) proposed in [18] we choose that defined by

$$k_1 = \varphi\left(\frac{1}{2}hA\right)\mathcal{F}(u^n), \quad (19)$$

$$k_2 = \varphi\left(\frac{1}{2}hA\right)\mathcal{F}\left(u^n + \frac{4}{3}hk_1\right), \quad (20)$$

$$u^{n+1} = u^n + h\left(\frac{13}{16}k_1 + \frac{3}{16}k_2\right), \quad (21)$$

because it minimizes the number of matrix–vector multiplications necessary to achieve third order accuracy. For analogous reasons, the specific fourth order formula (ETDR4) employed in the following is that given by

$$k_1 = \varphi\left(\frac{1}{2}hA\right)\mathcal{F}(u^n), \quad (22)$$

$$k_2 = \varphi\left(\frac{1}{2}hA\right)\left(\mathcal{F}(u^n) + \frac{1}{8}hAk_1\right), \quad (23)$$

$$k_3 = \varphi\left(\frac{1}{2}hA\right)\left(\mathcal{F}\left(u^n + \frac{3}{4}hk_2\right) - \frac{3}{4}hAk_2\right), \quad (24)$$

$$u^{n+1} = u^n + h\left(-\frac{43}{27}k_1 + 2k_2 + \frac{16}{27}k_3\right). \quad (25)$$

Table 1

Computational cost, C (CPU time in seconds of an Intel Quad-Core at 2.40 GHz processor), the evaluation of the linear $\mathcal{L}_0^{-1}\mathcal{L}$ versus the nonlinear $\mathcal{L}_0^{-1}\mathcal{N}$ operators. The radial resolution is N_r and L is the truncation parameter of the spherical harmonics expansion.

N_r	L	$C(\mathcal{L}_0^{-1}\mathcal{N})$	$C(\mathcal{L}_0^{-1}\mathcal{L})$
32	54	0.157	0.036
50	84	0.657	0.182
80	160	5.026	1.745

It should be remarked, however, that different choices could have to be made to guarantee a given convergence order also when an approximate Jacobian is employed, see e.g. the discussion in [26]. As will be seen in Section 5, we have only found this type of failure for the ETDR4 method, which has been therefore implemented by using Eq. (18).

We have also considered the ETDCox method of second order (ETDC2) of [17], which is a variant of a scheme introduced in [15,27]. This scheme can be defined setting $M = \mathcal{L}_0^{-1}\mathcal{L}$ and $N = \mathcal{L}_0^{-1}\mathcal{N}$. By multiplying Eq. (13) by the factor e^{-Mt} , and integrating over one time step h ,

$$u^{n+1} = e^{Mh}u^n + e^{Mh} \int_0^h e^{-M\tau} N(u(t_n + \tau)) d\tau, \tag{26}$$

is obtained.

Setting $N(u(t_n + \tau)) \approx N_n + \tau(N_n - N_{n-1})/h$, being $N_n = N(u(t_n))$, evaluated at $\tau = h/2$, gives the ETDC2 scheme:

$$u^{n+1} = e^{Mh}u^n + \left(e^{Mh} \int_0^h e^{-M\tau} d\tau \right) \frac{h}{2} (3N_n - N_{n-1}),$$

or

$$u^{n+1} = e^{Mh}u^n + \frac{h}{2} \varphi(Mh)(3N_n - N_{n-1}). \tag{27}$$

This scheme can be interpreted as an extension of the second order Adams–Bashforth method and can be extended to higher order along the same lines. The most attractive property of these schemes is that they are based only on matrix–vector products of the linear operator $\mathcal{L}_0^{-1}\mathcal{L}$. Computing them is significantly less demanding than computing the actions of the Jacobian required by ETDR methods, which entail repeated computation of the nonlinear terms. The difference in computational cost is displayed in Table 1. The number of nonlinear evaluations performed to advance one time level is the main shortcoming of the Rosenbrock methods for integrating the spectral thermal convection equations on spherical geometry.

The linear operators \mathcal{L} and A are represented by large matrices. The block-tridiagonal structure of \mathcal{L} is described in detail in the Appendix of [1]. Therefore, Krylov space methods based on the proposals of [11] can be conveniently employed to compute the exponential and related matrix functions that appear in the previous schemes. Notice that, employing the recipe proposed in [11], the computation of $\varphi(hA)$ can be achieved by computing the exponential of a bordered matrix. To evaluate the action of $\varphi(hA)$ on a vector v , needed by the ETDR schemes, we use the subroutine DGPVIV of the EXPOKIT package [23]. In this subroutine, a variable time-stepping strategy is implemented, in order to compute $w = \varphi(hA)v$ in a Krylov space of fixed dimension n_K by taking partial substeps. At each of them taken with an increment h_n , the norm of the error in the approximation of w at the current substep is estimated by ε_{loc} . Then the step is accepted if

$$\varepsilon_{loc} \leq 1.2h_n\varepsilon_{tol}, \tag{28}$$

with ε_{tol} a tolerance provided by the user, and 1.2 a safety factor which reduces the risk of rejecting the step. This strategy ensures that the accumulated global error is bounded by $1.2h\varepsilon_{tol}$ independently of the number of substeps taken.

Since we are interested in comparing with IMEX-BDF fixed time-step methods, the above strategy is modified to change the dimension of the Krylov subspace, n_K , instead of the time step, h_n , to satisfy the same condition given by Eq. (28). Then, the convergence will depend only on the value of h and ε_{tol} . In case of ETDC2, the subroutine DGPVIV allows the simultaneous computation of $e^{Mh}u^n$ and $\varphi(Mh)v^n$, with $v^n = 3N_n - N_{n-1}$. Again, only a fixed time-stepping strategy with variable Krylov dimension has been considered.

For analyzing the efficiency of ETD methods using Krylov spaces of dimension up to n_K , one has to keep in mind that, in order to advance one time step h , the number of evaluations of $A = \mathcal{J}(u^n)$ (in case of ETDR methods) or $M = \mathcal{L}_0^{-1}\mathcal{L}$ (in case of the ETDC2 method) is proportional to n_K . In contrast, for the IMEX-BDF methods, only one evaluation of the right hand side is required for each time step. Therefore, ETD methods need significantly larger time step than IMEX-BDF methods to be competitive.

Table 2

Ekman number, Rayleigh number, critical Rayleigh number, R_c , critical precession frequency, $|\omega_c|$, critical azimuthal wavenumber, m_c , radial resolution, N_r , spherical harmonics truncation, L , and number of equations, N , for the test solutions T_1 , T_2 , T_3 , T_{12} , and T_{13} , considered.

Case	T_1	T_2	T_3	T_{12}	T_{13}
E	10^{-4}	10^{-4}	10^{-4}	10^{-5}	10^{-6}
R	2.64×10^5	2×10^6	10^7	2.35×10^6	3.5×10^7
R_c	1.86×10^5	1.86×10^5	1.86×10^5	2.29×10^6	3.32×10^7
$ \omega_c $	5.06×10^2	5.06×10^2	5.06×10^2	2.37×10^3	1.10×10^4
m_c	6	6	6	11	23
N_r	32	50	80	50	80
L	54	84	160	84	160
N	281 263	1 083 650	6 143 119	1 083 650	6 143 119

Table 3

Values and intervals of the isosurfaces of the temperature, $T = T_c + \Theta$, the square of the modulus of the velocity field, $|\mathbf{v}|^2$, and the longitudinal component of the velocity, v_φ , plotted in Fig. 1 for the test solutions T_1 , T_2 , T_3 , T_{12} , and T_{13} , considered.

Case	T_1	T_2	T_3	T_{12}	T_{13}
T_{hot}	3.2×10^6	2×10^7	10^8	2.7×10^7	4.7×10^8
T_{cold}	1.7×10^6	1.3×10^7	6.2×10^7	1.5×10^7	2.2×10^8
$ \mathbf{v} ^2$	2.2×10^3	1.5×10^6	1.1×10^7	6.5×10^2	4.2×10^3
$ v_\varphi $	7.8	3.3×10^2	1.6×10^3	5.2	3.8×10^1
T_{min}	1.4×10^6	1.1×10^7	5.3×10^7	1.3×10^7	1.9×10^8
T_{max}	4.1×10^6	3.1×10^7	1.5×10^8	3.6×10^8	5.4×10^8
$ \mathbf{v} _{\text{min}}^2$	10^{-10}	3.8×10^{-5}	1.7×10^{-2}	8×10^{-13}	2×10^{-7}
$ \mathbf{v} _{\text{max}}^2$	1.6×10^4	7.8×10^6	5.6×10^7	1.5×10^3	1.7×10^4
$v_{\varphi \text{ min}}$	-9.8×10^1	-2.3×10^3	-7.4×10^3	-2.6×10^1	-8.4×10^1
$v_{\varphi \text{ max}}$	8.1×10^1	1.4×10^3	5.2×10^3	2.5×10^1	5.8×10^1

4. Numerical simulations

We have done several tests in order to compare the performance of the time integrators introduced above in different physical regimes described in [28]. In all the cases, the radius ratio is $\eta = 0.35$ and the Prandtl number $\sigma = 0.1$ estimated for the Earth's outer core.

To address the Rayleigh number dependence, we have considered three cases, denoted by T_1 , T_2 , and T_3 , respectively, where the Ekman number is taken to be fixed at $E = 10^{-4}$, while the values of the Rayleigh number increase according to the physical regime to be represented (see Table 2). In case T_1 (corresponding to S_2 in [6]), the solution is a weak supercritical quasi-periodic wave with $R = 1.42R_c$. In case T_2 (corresponding to S_3 in [6]), the solution, computed with moderate Rayleigh number $R = 10.78R_c$ is chaotic, but still maintains a recognizable columnar structure. Finally, a strongly supercritical and fully turbulent solution with $R = 53.58R_c$ is considered in case T_3 .

To address the Ekman number dependence, we have also considered cases T_{12} with $E = 10^{-5}$ and $R = 1.03R_c$ and T_{13} with $E = 10^{-6}$ and $R = 1.05R_c$. In both cases, the solution is a periodic traveling wave. The linear stability analysis for this range of parameters was performed in [29], where the power laws for the critical Rayleigh number, R_c , the absolute value of the critical precession frequency, $|\omega_c|$, and the critical azimuthal wavenumber, m_c , were found numerically. The Ekman numbers are in the range for which the power laws of the asymptotic E limit are satisfied. The critical values and spatial resolutions considered are shown in Table 2. Notice that the spatial resolutions are increased with the complexity of the solution, and in order to resolve the small scale structures which appear in the turbulent solution T_3 or that of the lowest E (T_{13}), $N = 6143119$ equations must be integrated. The analysis of the resolutions required to reproduce the dynamics of the flow in each regime is discussed in [28].

The isosurfaces of the temperature $T = T_c + \Theta$, $|\mathbf{v}|^2$, and v_φ of the initial conditions of T_i , $i = 1, 2, 3, 12, 13$, are shown in Fig. 1. For each scalar field the values where the isosurfaces are taken and their limits are written down in Table 3. Cases T_1 , T_{12} and T_{13} resemble very much the eigenfunctions of the linear problem. There are m_c spiraling convective columns which are parallel to the axis of rotation, so nearly fulfilling the Taylor–Proudman theorem. As it is well known when E is decreased, m_c increases, the spiraling of the columns is more pronounced, and the columns are confined in a thin cylindrical layer near the inner boundary.

For the solution T_2 displayed in the second row, the contribution of the zonal flow to the kinetic energy density is maximum and advective effects deform the temperature isosurfaces, but its velocity field already maintains a roughly columnar structure. The third row corresponds to T_3 . The reflection symmetry with respect to the equator is clearly broken, and the strong turbulent convection fills the spherical shell. Although the mean zonal flow maintains its strength, its ratio to the convective part has decreased.

To make the comparisons, all the test runs have been initialized starting from the initial conditions shown in Fig. 1. In cases T_1 , T_2 and T_3 , the initial conditions are obtained from a sequence of solutions obtained with lower R after the initial transients are discarded and until a stationary pattern is reached, or until the time-averaged properties and the fundamental

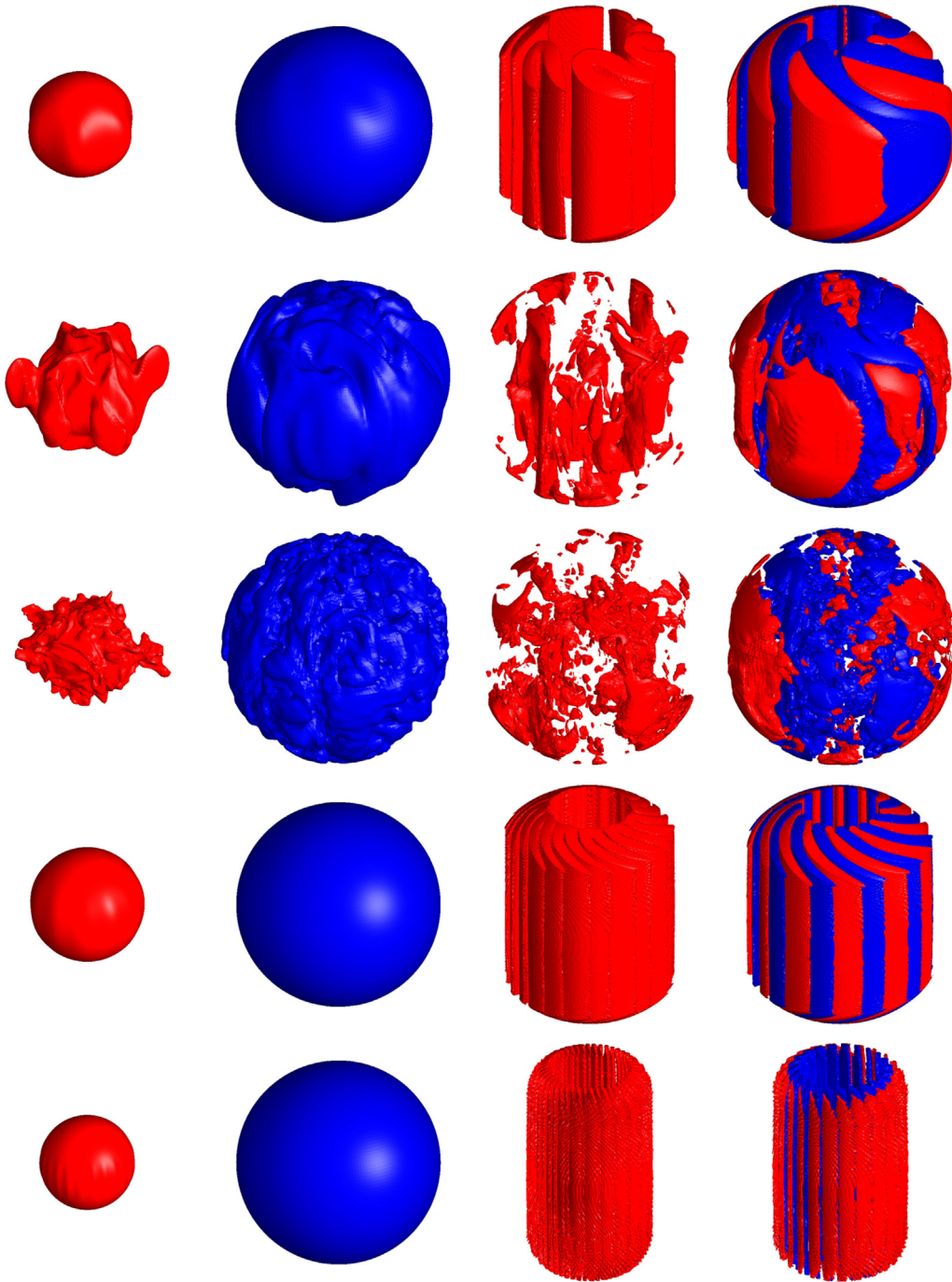


Fig. 1. From left to right, snapshots of the isosurfaces of the temperature T (hot and cold respectively), of $|v|^2$ and of v_φ . For the latter, red/blue means positive/negative values. First row: Case T_1 ($E = 10^{-4}$ and $R = 2.64 \times 10^3$). Second row: Case T_2 ($E = 10^{-4}$ and $R = 2 \times 10^6$). Third row: Case T_3 ($E = 10^{-4}$ and $R = 10^7$). Fourth row: Case T_{12} ($E = 10^{-5}$ and $R = 2.35 \times 10^6$). Last row: Case T_{13} ($E = 10^{-6}$ and $R = 3.5 \times 10^7$). (For interpretation of the references to color in this figure legend, the reader is referred to the web version of this article.)

frequencies do not change more than 1%. The first solution of the sequence is at $R = 2 \times 10^5$ and it is computed by starting from an initial condition with velocity $\mathbf{v} = \mathbf{0}$, and temperature

$$T_B(r, \theta, \varphi) = \frac{r_i r_o}{r} - r_i + \frac{2A}{\sqrt{2\pi}} (1 - x^2)^3 P_m^m(\theta) \cos m\varphi, \tag{29}$$

where $A = 0.1$, $x = 2r - r_i - r_o$, $m = 6$, and

Table 4

Frequency of maximum amplitude f_{max} , mean frequency f_{mean} , mean period P_{mean} , dimensional mean period $P_d = P_{mean}d_c^2/\nu$ ($d_c = 2.3 \times 10^6$ m and $\nu = 10^{-6}$ m²/s corresponding to values of the Earth's outer core) and final time t_f (at which errors $\varepsilon(u)$ are computed) for all the cases considered.

Case	f_{max}	f_{mean}	P_{mean}	P_d (years)	t_f
T_1	59.11247	58.58775	1.706841×10^{-2}	2.9×10^9	10^{-1}
T_2	48.31012	872.7377	1.145820×10^{-3}	1.9×10^8	10^{-2}
T_3	168.9822	1187.499	8.421060×10^{-4}	1.4×10^8	10^{-4}
T_{12}	367.5766	368.5130	2.713608×10^{-3}	4.56×10^8	10^{-3}
T_{13}	1539.483	1539.483	6.495687×10^{-4}	1.1×10^8	3.25×10^{-4}

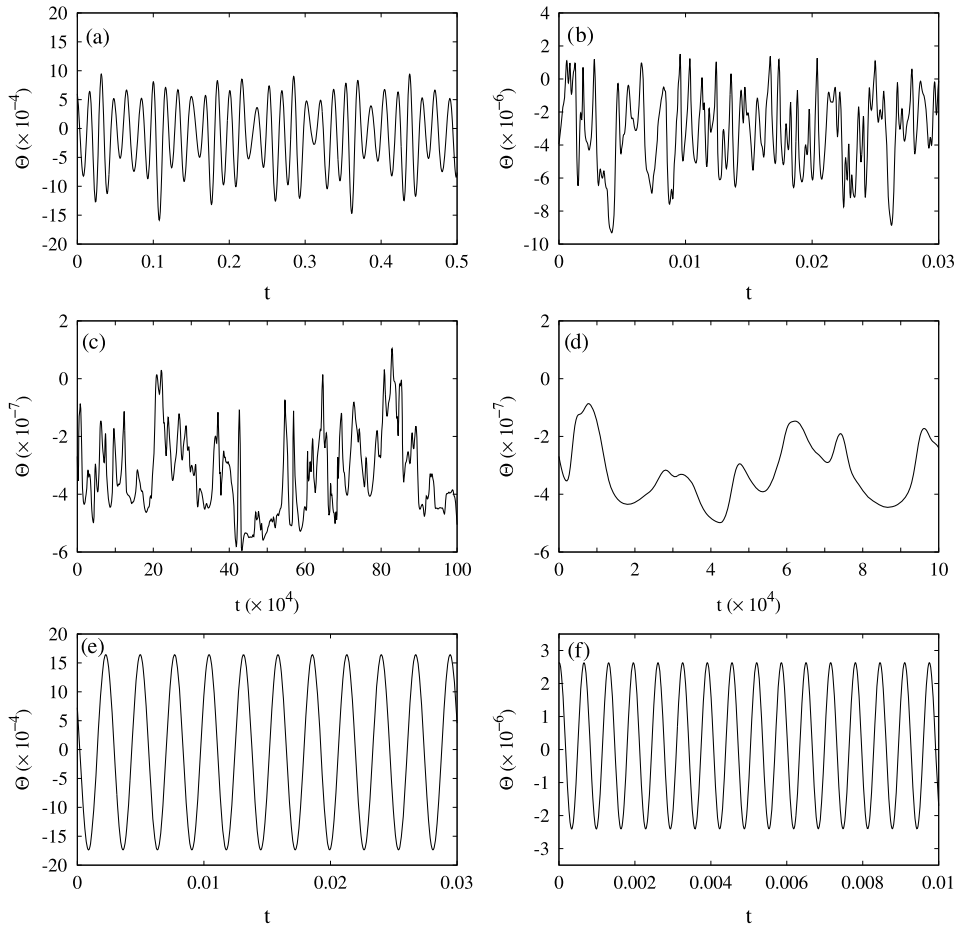


Fig. 2. Temperature perturbation $\Theta(r_i + (r_o - r_i)/7, 0, 3\pi/8)$ plotted versus time for (a) T_1 , (b) T_2 , (c) T_3 , (d) detail of (c), (e) T_{12} , and (f) T_{13} .

$$P_m^m(\theta) = \sqrt{(2m+1)!!/2(2m)!!} \sin^m \theta$$

is the normalized associated Legendre function of order and degree m . As it is said the solution tends, after an abrupt transient, to the above mentioned azimuthal traveling wave of wavenumber $m = 6$. For $E = 10^{-5}$ (case T_{12}), the first solution is computed using the same initial condition, but with critical wavenumber $m = 11$, and at $E = 10^{-6}$ (case T_{13}) with $m = 23$.

In Table 4, some quantities are shown to give some idea of the time scales corresponding to the different cases considered. The frequency f_{max} with maximum amplitude A_{max} of the frequency spectrum (f_i, A_i), the mean frequency $f_{mean} = \sum A_i f_i / \sum A_i$, the mean period $P_{mean} = 1/f_{mean}$ and the dimensional mean period $P_d = P_{mean}d_c^2/\nu$ with $d_c = 2.3 \times 10^6$ m and $\nu = 10^{-6}$ m²/s, corresponding to estimations of values for the Earth's outer core. The system is evolved from the initial condition to a final time t_f which is given in the same table. It covers several mean periods of the orbit for T_1 and T_2 . However, for T_3 , T_{12} and T_{13} , only a fraction of the mean period is considered, to avoid too long time integrations. We have checked for T_{12} that the choice of a larger t_f does not alter substantially the behavior of the time integration methods.

The time series of the temperature perturbation Θ at the point $(r_i + (r_o - r_i)/7, 0, 3\pi/8)$ are shown in Figs. 2(a)–(f), for all the tests. The smooth oscillatory nature of cases T_1 , T_{12} , and T_{13} with very different periods, and the chaotic temporal

dependence of T_2 and T_3 can be clearly distinguished. The time interval is similar to t_f only for T_1 and T_2 . For the rest (T_3 , T_{12} , and T_{13}) the time interval is between one and two orders of magnitude larger. Fig. 2(d) shows, for T_3 , a detail of the oscillations with a time interval 10 times larger than t_f .

To check the efficiency of the different schemes, the relation between the relative error, the time step h , and the run time is analyzed. The former is defined as

$$\varepsilon(u) = \frac{\|u - u_r\|_2}{\|u_r\|_2}, \quad (30)$$

where u is the solution we want to check, and u_r is an accurate reference solution obtained with the Q -implicit variable size and variable order method of [1]. More precisely, u_r is obtained with absolute and relative error tolerances $\varepsilon^a = \varepsilon^r$ (see [1]), equal to 10^{-13} for T_1 , to 10^{-11} for T_2 , T_3 and T_{13} , and to 10^{-12} for T_{12} . The decrease of the relative error given by Eq. (30) is achieved by decreasing the step size h in the case of the IMEX method and also by decreasing the tolerances ε_{tol} (see Eq. (28)) for the local errors (coming from the Krylov approximation) in the case of the ETD methods. Notice that the errors computed in this way are to be interpreted as empirical estimates of the time discretization error, while no attempt here is made to estimate the error due to the space discretization method.

For the IMEX-BDF methods the curves of relative error $\varepsilon(u)$ versus h are extended to the right, up to the maximum h allowed by stability. In the case of ETD methods the limitations on the maximum time step are due to an increase in the Krylov dimension n_K used to approximate the exponentials. It was limited to $n_K \leq 50$.

4.1. Rayleigh number dependence

In this subsection, the influence of the Rayleigh number on the performance of the time integration methods is studied by considering the cases T_i , $i = 1, 2, 3$. Figs. 3(a), (c), (e) show $\varepsilon(u)$ versus h for the methods described in Section 3. These three plots suggest that:

- For a given time step h , the ETD methods are always much more accurate than the corresponding IMEX-BDF methods of the same order. ETD2 gives values of $\varepsilon(u)$ similar to those of the IMEX-BDF3, while ETD3 gives errors similar to those of IMEX-BDF5. As the Rayleigh number increases, the ETD methods become even more accurate.
- ETD2 is about one order of magnitude less accurate than ETD2 for T_1 . At moderate and high supercritical conditions (T_i , $i = 1, 2$) the accuracy of the former degrades, and its behavior and that of IMEX-BDF2 are nearly the same; most likely because their treatment of the nonlinear terms is very similar.
- For the three cases under consideration and a given time step h , all the ETD methods use similar values of the Krylov dimension n_K . They range from 2–5 for the smallest h , up to 20–30 for the highest. For larger h than those shown in Figs. 3(a), (c), (e) the increase of the Krylov dimension employed is more pronounced.
- ETD k methods of orders $k = 3, 4$ are, in general, much more accurate than those of second order. However, for T_1 the accuracy of ETD4 is very similar to ETD3. The order of the latter is exhibited for the smallest h , while for the larger the slopes of the ETD3 and ETD4 error curves in Fig. 3(a) are very similar. With increasing R the differences in accuracy between both methods are more pronounced (Figs. 3(c) and (e)).

Figs. 3(b), (d), (f) show $\varepsilon(u)$ versus the run time, rt , for T_1 , T_2 , and T_3 , respectively. These three plots suggest that:

- When comparing IMEX-BDF and ETD methods, it must be kept in mind that to advance one time step IMEX-BDF methods only require one linear solve (equivalent in cost to a linear evaluation) and one computation of the nonlinear terms, while ETD methods need $O((k-1)n_K)$ evaluations of the linear and nonlinear terms if an approximated Jacobian (see Eq. (17)) is employed. If instead the exact Jacobian (Eq. (18)) is employed, the number of evaluations per time step is $O(2(k-1)n_K)$. ETD2 is more efficient than ETD methods because they only perform one evaluation of the nonlinear terms and $O(n_K)$ of the linear, which are cheaper to perform.
- Taking the previous point into account, in order to obtain solutions with similar $\varepsilon(u)$ at similar costs, the time step h_{ETDRk} of the ETD k method should be $O((k-1)n_K)$ times larger than h_{BDFk} , required for the IMEX-BDF k methods. This does not happen for T_i , $i = 1, 2, 3$, and thus IMEX-BDF methods are more efficient to obtain moderately accurate solutions at $E = 10^{-4}$ for the wide range of R explored. However, the difference $h_{ETDRk} - h_{BDFk}$ increases slightly with increasing R .
- The most accurate IMEX-BDF fixed step method (IMEX-BDF5) can achieve relative errors $\varepsilon(u)$ down to $O(10^{-10})$, $O(10^{-5})$ and $O(10^{-8})$, for T_1 , T_2 , and T_3 , respectively. The most accurate solutions using ETD4 have $\varepsilon(u)$ down to $O(10^{-12})$, $O(10^{-7})$ and $O(10^{-12})$. The differences in accuracy between the most accurate solution obtained with IMEX-BDF5 and that obtained with ETD4 increase as R is increased. In all the three test cases, the VSVO Q -implicit method of [1] (of orders from 2 up to 5), with very low tolerance values, can obtain the same accuracy as the ETD methods but more efficiently.

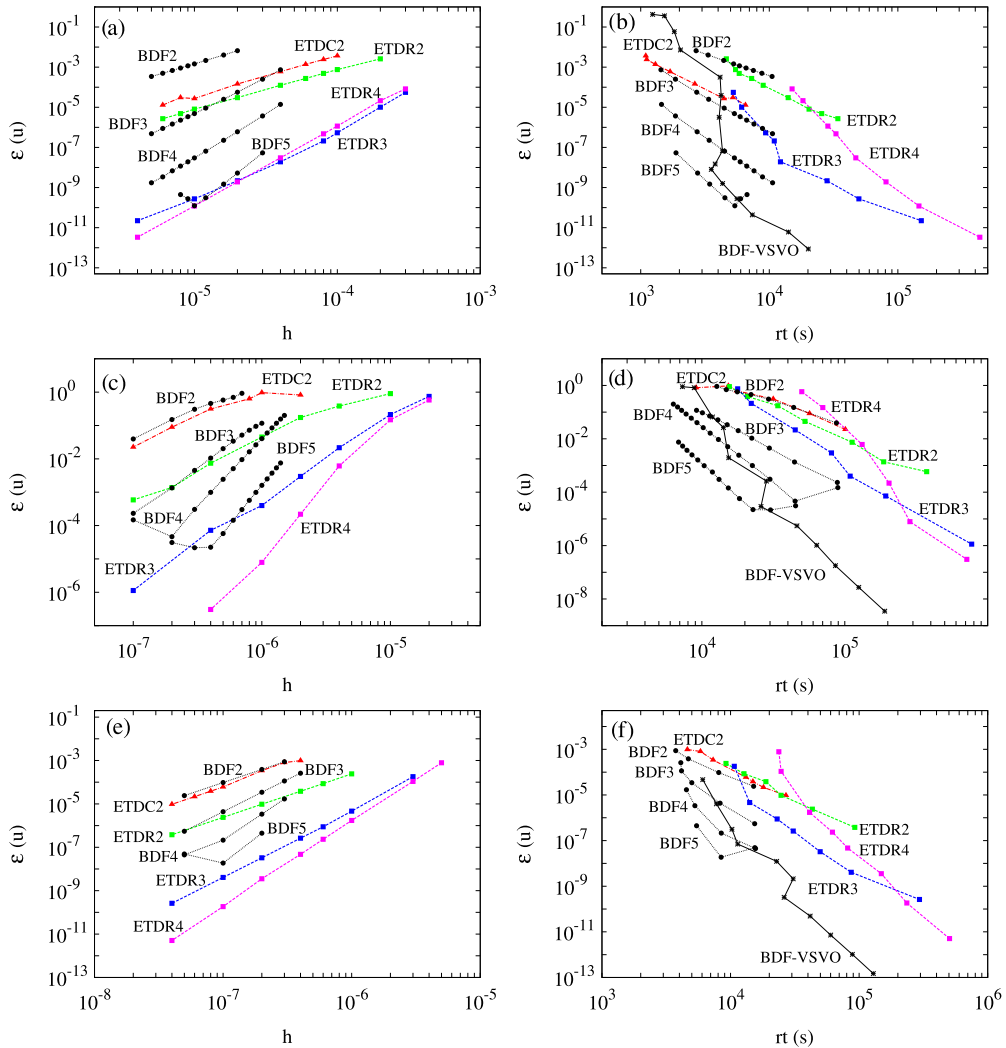


Fig. 3. (a) The relative error, $\varepsilon(u)$, plotted versus the constant time step h for the ETD and IMEX methods and the case T_1 . (b) The relative error, $\varepsilon(u)$, plotted versus the run time in seconds for the same methods shown in (a) and the case T_1 . (c) Same as (a) but for the case T_2 . (d) Same as (b) but for the case T_2 . (e) Same as (a) but for the case T_3 . (f) Same as (b) but for the case T_3 . The symbols and types of lines indicate: IMEX-BDF (\bullet , dotted line), IMEX-BDF-VSVO ($*$, solid line), ETDC2 (\blacktriangle , dash-dotted line (red)), ETDRk (\blacksquare , dashed line ($k=2$ green, $k=3$ blue and $k=4$ magenta)). The orders of the methods are labeled on the curves. (For interpretation of the references to color in this figure legend, the reader is referred to the web version of this article.)

4.2. Ekman number dependence

In this subsection, the influence of the Ekman number on the performance of the time integration methods is studied by considering the cases T_1 and T_{1i} , $i = 2, 3$. Fig. 3(a) and Figs. 4(a), (c) show the relative error $\varepsilon(u)$ plotted versus the time step h for the methods described in Section 3. These three plots suggest that:

- As for the R dependence, for a given time step h , the ETDR methods are always much more accurate than the corresponding IMEX-BDF methods of the same order. As E decreases, the ETDR methods become even more accurate. This is quantified in Table 5 where the constants C_{meth} of the numerical fits $\varepsilon(u) = C_{meth}h^k$ are shown. For instance, notice that at the lowest E (case T_{13}) the constant for the ETDR3 method (the highest order taken for which the approximate Jacobian can be used) is more than 5 orders of magnitude smaller than that of the IMEX-BDF3.
- ETDC2 is roughly one order of magnitude less accurate than ETDR2, but one order of magnitude more accurate than IMEX-BDF2 for the three E considered. This is one of the reasons for which ETDC2 is the more efficient option (as will be shown later) among the second order methods.
- As happened when addressing the R dependence, for the three cases under consideration and a given time step h , all the ETD methods use similar values of the Krylov dimension n_K . They range from 2–5 for the smallest h , up to 20–30 for the largest. It is nearly 40 for the largest h in cases T_{1i} , $i = 2, 3$, and ETDRk of orders $k = 3, 4$.

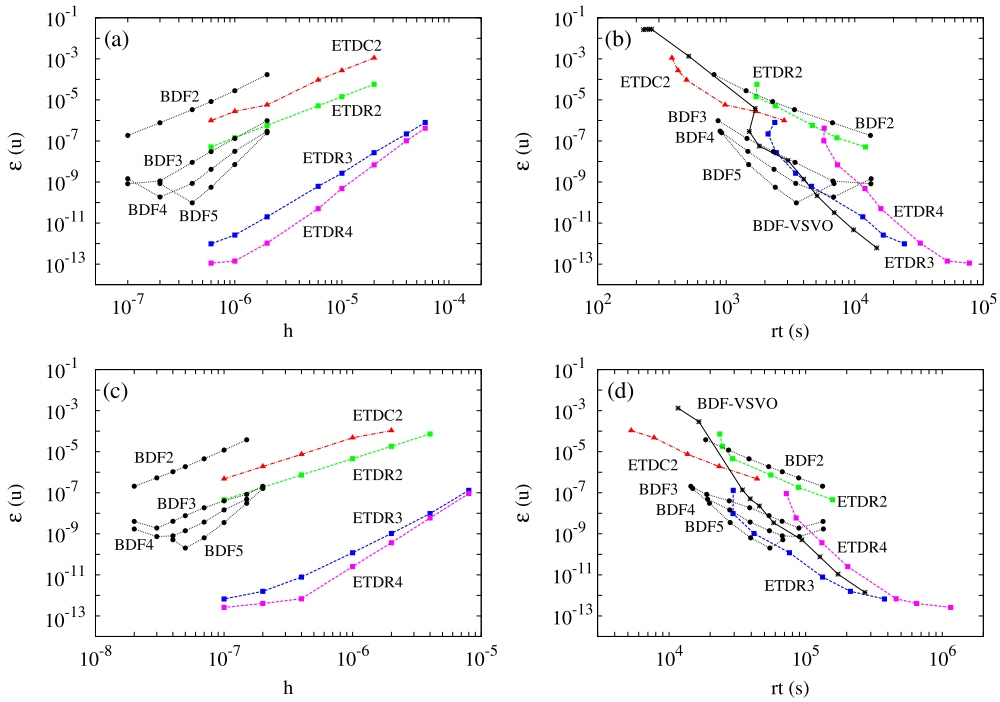


Fig. 4. (a, c) Relative error, $\varepsilon(u)$, plotted versus the constant time step, h , for ETD and IMEX-BDF methods for the cases T_{12} ($E = 10^{-5}$) and T_{13} ($E = 10^{-6}$), respectively. (b, d) Relative error plotted versus the run time, rt , in seconds for the same methods and cases shown in (a) and (c). The symbols and types of lines are those of Fig. 3.

- The facts that the Krylov dimension does not depend on E , (and neither on R) for the range of $\varepsilon(u)$ shown in the plots, and that the constants C_{meth} are much larger for IMEX-BDF than for the ETDR suggest that the latter would be more efficient for integrating flows at $E \leq 10^{-6}$.
- The vertical distance between the ETDR2 and ETDR3 (or ETDR4) curves of Fig. 3(a) and Figs. 4(a), (c) increases as E decreases. This can be seen by measuring the difference between $\varepsilon(u)$ for ETDR2 and ETDR3 at, for instance, $h = 10^{-4}$, $h = 10^{-5}$, and $h = 10^{-6}$, and T_1 , T_{12} , and T_{13} , respectively. In the latter case the vertical distance is the largest. This suggest that high order (> 2) ETDR methods would be suitable at low E .
- In the case of the IMEX-BDF methods, as E is decreased the differences in accuracy (vertical distance) between the methods with orders $k = 3, 4, 5$ diminish. The range of h in which the curves are obtained without a noticeable accumulation of round-off errors (h for which $\varepsilon(u)$ versus h has positive slope) also decreases with E . This suggest that as E is decreased fixed step and order IMEX-BDF methods with order larger than 3 would not improve substantially the accuracy. Moreover, selecting a time step h belonging to the region of absolute stability and without accumulation of round-off errors would be more difficult as E is decreased.

Fig. 3(a) and Figs. 4(b), (d) show the relative error $\varepsilon(u)$ plotted versus the run time for the cases T_1 and T_{1i} , $i = 2, 3$. These three plots suggest that:

- As discussed in the previous subsection, in order to obtain solutions with similar $\varepsilon(u)$ at similar costs, the time step h_{ETDRk} of the ETDR k method should be $O((k-1)n_K)$ times larger than h_{BDFk} , required for the IMEX-BDF k methods. This appears to happen at the lowest Ekman number $E = 10^{-6}$ (case T_{13}) and thus IMEX-BDF methods are more efficient only for obtaining moderately accurate solutions at the moderately low Ekman numbers $E = 10^{-4}, 10^{-5}$.
- The differences between h_{BDFk} and h_{ETDRk} have stronger dependence on the decrease of E than on the increase of R as in the previous subsection.
- The ETDC2 method is in general the most efficient among the second order methods for the three cases. This is because ETDC2 method retains the most attractive properties of the other two. It only requires one evaluation of the nonlinear terms at each time step (as IMEX-BDF2) and the solution of the linear part is only constrained by the Krylov approximation of the exponential (as for ETDR2).
- Implementations of higher order linear multistep exponential methods similar to ETDC2 could be competitive, but would require the computation of the functions $\varphi_j(z) = (\varphi_{j-1} - 1/j!)/z$ with $j > 1$, whose numerical approximation is known to lead often to cancellation errors [30].
- As in the case of increasing R , when E is decreased, very accurate solutions can only be obtained with fixed-time step by using ETDR methods of order $k = 3, 4$ or the VSVO Q -implicit method [1] with very low tolerances. At the lowest E ,

Table 5

Least-squares fits for the constant C in $\varepsilon(u) = Ch^k$, where $k = 2, 3, 4, 5$ is the order of the method, as a function of the Ekman number E . The statistical errors of the fit are less than 5%, and for ETD methods less than 1%.

Method	$E = 10^{-4}$	$E = 10^{-5}$	$E = 10^{-6}$
ETDC2	3.7×10^5	2.7×10^6	4.7×10^7
ETDR2	7.6×10^4	1.4×10^5	4.6×10^6
ETDR3	3.0×10^5	3.7×10^6	1.5×10^8
ETDR4	1.3×10^{10}	3.1×10^{10}	2.3×10^{13}
IMEX-BDF2	1.6×10^7	2.3×10^7	7.1×10^8
IMEX-BDF3	4.3×10^9	1.2×10^{11}	5.5×10^{13}
IMEX-BDF4	3.0×10^{12}	3.1×10^{16}	1.5×10^{20}
IMEX-BDF5	1.6×10^{15}	7.9×10^{21}	4.1×10^{26}

due to the large number of time steps required for the IMEX-BDF-VSVO method to achieve such high accuracy, the ETDR3 method becomes more efficient because it can employ a time step generally larger than the average time step of the IMEX-BDF-VSVO method.

Using the numerical fit $\varepsilon(u) = C_{meth}h^k$, and assuming that $C_{meth} = C_{meth}(E)$ (shown in Table 5), values of C_{meth} can be extrapolated for regimes near the onset of convection for integrations over half a period of the solution. We use the constants $C_{meth}(E)$ of the methods of third order (since they are the most efficient among the ETDRs) and $E = 10^{-5}, 10^{-6}$ (cases $T_{1i}, i = 2, 3$) to make an extrapolation of $C(E_{core})$ for $E_{core} = 2.6 \times 10^{-15}$.

We have fitted a potential law, $C_{meth} = aE^b$, to cases $T_{1i}, i = 2, 3$ because both are traveling waves, which near to the onset of convection are confined near the inner core (see Fig. 1), and it is known that critical parameters R_c, ω_c and m_c follow this kind of dependence. With the parameters σ and η corresponding to those widely used for the Earth's outer core the critical frequency is $\omega_c = 1.1E^{-0.66}$ [29], and taking into account $E_{core} = 2.6 \times 10^{-15}$, an approximate period $T = 10^{-9}$ is obtained. In dimensional units it would be $T = 7 \times 10^9$ s. This value matches well with long period oscillations (> 100 years) of the inner core estimated in [31]. In addition most of the physical properties and time scales in developed turbulent convection follow this type of law [28,32].

For ETDR3 and IMEX-BDF3, $C_{ETDR3} = 0.3E^{-1.6}$ and $C_{BDF3} = 6 \times 10^{-3}E^{-2.7}$ are obtained, respectively. By taking into account $E_{core} = 2.6 \times 10^{-15}$, the constants are $C_{ETDR3} = 7 \times 10^{22}$ for ETDR3 and $C_{BDF3} = 10^{37}$ for IMEX-BDF3. This result implies that for integrating half a period (roughly $t_f = 5 \times 10^{-10}$ adimensional time units) of the first bifurcated traveling wave at the Earth's outer core conditions, with relative error $\varepsilon(u) = 10^{-6}$, the time step needed using ETDR3 and IMEX-BDF3 would be approximately 2×10^{-10} and 5×10^{-15} , respectively. If the Krylov dimension required by the ETDR methods does not depend strongly on E to obtain solutions with a given value of $\varepsilon(u)$, as suggested by our results, the ETDR methods could be the most efficient option for integrating flows near the Earth's outer core conditions.

5. Numerical issues in the application of exponential methods

In this section, some implementation issues of the exponential methods are addressed. The details discussed are in general common to all the test cases, so only the computational aspects of the case T_1 will be commented.

In Fig. 5(a) the relative error $\varepsilon(u)$ is plotted versus the constant time step h for the ETD methods. For each h , the Krylov dimension n_K used to approximate the exponentials is labeled in the curves. For a given h , the values of n_K selected for the different methods are very similar. The greatest differences (about 5) are between ETDC2 and ETDR methods and the larger time steps, for which n_K are larger. As h decreases, n_K decreases too, from approximately 25 down to 5, and also the bound for the local relative error, $b_{loc}(u) = 1.2h\varepsilon_{tol}\|u_r\|^{-1}$ (computed from Eq. (28)), used in the Krylov approximation. This bound is shown in Fig. 5(b) as a function of h for the solutions in Fig. 5(a). As it is expected $b_{loc}(u)$ must be decreased accordingly with the order of the integration. This can be seen in the curves for the third and fourth order ETDR methods. The oscillations are due to the way we have modified ε_{tol} when changing h . In the case of second order we were conservative for the larger h , and therefore the slope is less than two.

Finally, Fig. 5(c) shows $\varepsilon(u)$ versus the parameter ϵ used in the one-sided finite difference approximation of the Jacobian, for the Rosenbrock methods of Fig. 5(a) with $h = 10^{-4}$. The horizontal straight lines are the values of $\varepsilon(u)$ obtained with the centered exact formula. As the order of the method increases, the range of values of ϵ which can be used in the one-sided approximation, giving the same result, decreases. For the second and third order methods the value selected in our tests, $\epsilon = \|u(0)\|_2 \sqrt{\epsilon_{mach}}$, is always in this range. In the case of the fourth order method the one-sided approximation always gives a larger $\varepsilon(u)$ than that obtained with the exact computation of the Jacobian, as the theoretical results in [18] (Theorem 5.1) suggest.

6. Conclusions and open issues

In this work, we have carried out an assessment of the accuracy and efficiency of several exponential time integration methods coupled to a spectral discretization of the three-dimensional Boussinesq thermal convection equations in rotating

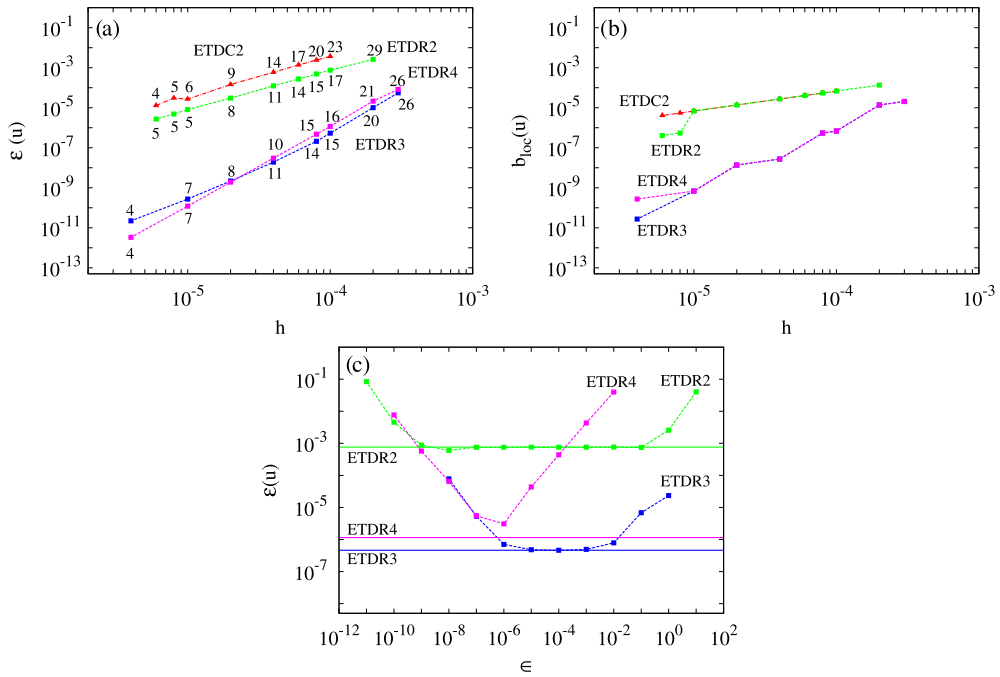


Fig. 5. (a) The relative error, $\epsilon(u)$, versus the constant time step, h . The numeric labels indicate the Krylov dimension. (b) Bound for the local relative error used in the Krylov approximation, $b_{loc}(u) = 1.2h\epsilon_{tol}\|u_r\|^{-1}$, versus h . (c) $\epsilon(u)$ versus the tolerance ϵ used in the one-sided approximation of the Jacobian for $h = 10^{-4}$. For each method the straight lines indicate the $\epsilon(u)$ obtained with the centered formula. All the plots correspond to the ETD methods and case T_1 . The symbols and types of lines indicate: ETDC2 (\blacktriangle , dash-dotted line (red)), ETDRk (\blacksquare , dashed line ($k = 2$ green, $k = 3$ blue and $k = 4$ magenta)), (For interpretation of the references to color in this figure legend, the reader is referred to the web version of this article.)

spherical shells. Fixed time-step exponential and IMEX-BDF methods have been compared. The latter were already studied in [1,6]. We have focused especially on the application of the so called exponential Rosenbrock methods proposed in [18].

A wide range of numerical simulations have shown clearly that, for a given convergence order, such exponential methods are more accurate by at least one order of magnitude than equivalent order IMEX-BDF schemes. This is especially true when they are employed with large time steps and at low Ekman number. The computational cost per time step is, in general, higher than that of the equivalent order IMEX-BDF scheme, at least for the present implementation. However, in the small Ekman number limit, exponential Rosenbrock methods tend to be competitive also in terms of computational cost, even compared with the VSVO implementation of the IMEX-BDF.

These conclusions appear to be very promising for their application, since this is the physically relevant regime for mantle and core convection problems. Future developments will address a number of computational issues, such as the full parallelization of the present serial implementation, and the reduction of the computational cost per time step by application of different approaches for the computation of the exponential matrix, such as e.g. those proposed in [33,34].

Acknowledgements

The research of F.G., M.N. and J.S. has been supported by the Spanish Ministerio de Ciencia e Innovación, and Generalitat de Catalunya under projects MTM2010-16930 and 2009-SGR-67, respectively. This work was started during a visit of F.G. at MOX – Politecnico di Milano, with financial support from the INDAM-GNCS project *Metodologie teoriche ed applicazioni avanzate nei metodi Semi-Lagrangiani*. F.G. would like to thank A. Quarteroni and L. Formaggia for the kind invitation at MOX. Useful conversations with P. Novati and M. Restelli are also kindly acknowledged.

References

- [1] F. Garcia, M. Net, B. García-Archilla, J. Sánchez, A comparison of high-order time integrators for thermal convection in rotating spherical shells, *J. Comput. Phys.* 229 (2010) 7997–8010.
- [2] W. Bourke, A multi-level spectral model: Formulation and hemispheric integrations, *Mon. Weather Rev.* 102 (1974) 688–701.
- [3] J.P. Boyd, *Chebyshev and Fourier Spectral Methods*, Dover, New York, 1999.
- [4] C. Canuto, M.Y. Hussaini, A. Quarteroni, T.A. Zang, *Spectral Methods. Fundamentals in Single Domains*, Springer-Verlag, Berlin, Heidelberg, 2006.
- [5] B.J. Hoskins, A.J. Simmons, A multi-layer spectral model and the semi-implicit method, *Q. J. R. Meteorol. Soc.* 101 (1975) 637–655.
- [6] F. Garcia, M. Net, J. Sánchez, A comparison of high-order time integrators for highly supercritical thermal convection in rotating spherical shells, in: *Spectral and High Order Methods for Partial Differential Equations – ICOSAHOME 2012*, in: M. Azaiez, H. El Fekih, J.S. Hesthaven (Eds.), *Lecture Notes in Computational Science and Engineering*, vol. 95, 2014.
- [7] U. Ascher, S. Ruuth, B. Wetton, Implicit–explicit methods for time-dependent partial differential equations, *SIAM J. Numer. Anal.* 32 (3) (1995) 797–823.

- [8] E. Hairer, G. Wanner, Solving Ordinary Differential Equations. II. Stiff and Differential–Algebraic Problems, Springer, 1991.
- [9] D. Lawson, Generalized Runge–Kutta processes for stable systems with large Lipschitz constants, *SIAM J. Numer. Anal.* 4 (1967) 372–380.
- [10] C. Moler, C.V. Loan, Nineteen dubious ways to compute the exponential of a matrix, twenty-five years later, *SIAM Rev.* 45 (2003) 3–46.
- [11] Y. Saad, Analysis of some Krylov subspace approximations to the matrix exponential operator, *SIAM J. Numer. Anal.* 29 (1992) 209–228.
- [12] A. Martinez, L. Bergamaschi, M. Caliari, M. Vianello, A massively parallel exponential integrator for advection–diffusion models, *J. Comput. Appl. Math.* 231 (2009) 82–91.
- [13] J.C. Schulze, P.J. Schmid, J.L. Sesterhenn, Exponential time integration using Krylov subspaces, *Int. J. Numer. Methods Fluids* 60 (2009) 591–609.
- [14] R. Archibald, K. Evans, J. Drake, J.B. White III, Multiwavelet discontinuous Galerkin-accelerated exact linear part (ELP) method for the shallow water equations on the cubed sphere, *Mon. Weather Rev.* 139 (2011) 457–473.
- [15] S.M. Cox, P.C. Matthews, Exponential time differencing for stiff systems, *J. Comput. Phys.* 176 (2002) 430–455.
- [16] M. Hochbruck, A. Ostermann, On Krylov subspace approximations to the matrix exponential operator, *Acta Numer.* 19 (2010) 209–286.
- [17] P.W. Livermore, An implementation of the exponential time differencing scheme to the magnetohydrodynamic equations in a spherical shell, *J. Comput. Phys.* 220 (1) (2007) 824–838.
- [18] M. Hochbruck, C. Lubich, H. Selhofer, Exponential integrators for large systems of differential equations, *SIAM J. Sci. Comput.* 19 (5) (1998) 1552–1574.
- [19] G. Glatzmaier, Numerical simulations of stellar convective dynamos. I. The model and method, *J. Comput. Phys.* 55 (1984) 461–484.
- [20] A. Tilgner, Spectral methods for the simulation of incompressible flow in spherical shells, *Int. J. Numer. Methods Fluids* 30 (1999) 713–724.
- [21] C.F. Curtiss, J.O. Hirschfelder, Integration of stiff equations, *Proc. Natl. Acad. Sci. USA* 38 (1952) 235–243.
- [22] M. Hochbruck, C. Lubich, On Krylov subspace approximations to the matrix exponential operator, *SIAM J. Numer. Anal.* 34 (5) (1997) 1911–1925, <http://dx.doi.org/10.1137/S0036142995280572>.
- [23] R.B. Sidje, Expokit: A software package for computing matrix exponentials, *ACM Trans. Math. Softw.* 24 (1) (1998) 130–156.
- [24] J. Sánchez, M. Net, B. García-Archilla, C. Simó, Newton–Krylov continuation of periodic orbits for Navier–Stokes flows, *J. Comput. Phys.* 201 (1) (2004) 13–33.
- [25] E. Hairer, H.P. Norsett, G. Wanner, Solving Ordinary Differential Equations. I. Nonstiff Problems, 2nd revised edition, Springer-Verlag, 1993.
- [26] P. Novati, On the construction of restricted-denominator exponential W-methods, *J. Comput. Appl. Math.* 221 (2008) 86–101.
- [27] G. Beylkin, J.M. Keiser, L. Vozovoi, A new class of time discretization schemes for the solution of nonlinear PDEs, *J. Comput. Phys.* 147 (1998) 362–387.
- [28] F. Garcia, J. Sánchez, M. Net, Numerical simulations of high-Rayleigh-number convection in rotating spherical shells under laboratory conditions, *Phys. Earth Planet. Inter.* (2014), submitted for publication.
- [29] F. Garcia, J. Sánchez, M. Net, Antisymmetric polar modes of thermal convection in rotating spherical fluid shells at high Taylor numbers, *Phys. Rev. Lett.* 101 (2008) 194501.
- [30] J. Niesen, W.M. Wright, Algorithm 919: A Krylov subspace algorithm for evaluating the φ -functions appearing in exponential integrators, *ACM Trans. Math. Softw.* 38 (3) (2012) 22:1–22:19.
- [31] M. Dumberry, J. Mound, Inner core–mantle gravitational locking and the super-rotation of the inner core, *Geophys. J. Int.* 181 (2010) 806–817.
- [32] U. Christensen, Zonal flow driven by strongly supercritical convection in rotating spherical shells, *J. Fluid Mech.* 470 (2002) 115–133.
- [33] P. Novati, Using the restricted-denominator rational Arnoldi method for exponential integrators, *SIAM J. Matrix Anal. Appl.* 32 (2011) 1537–1558.
- [34] A. Al-Mohy, J. Higham, Computing the action of the matrix exponential, with application to exponential integrators, *SIAM J. Sci. Comput.* 33 (2) (2011) 488–511.